The 10th JFPS International Symposium on Fluid Power FUKUOKA 2017 Oct. 24-27, 2017 JFPS The Japan Fluid Power System Society

MATHEMATICAL MODELING OF A PNEUMATIC VANE MOTOR IN MATLAB/SIMULINK

Stephan MERKELBACH*, Joan Vidal MAS* and Hubertus MURRENHOFF*

*Institute for Fluid Power Drives and Controls (IFAS), RWTH Aachen University
Steinbachstr. 53, 52074 Aachen, Germany
(E-mail: stephan.merkelbach@ifas.rwth-aachen.de)

Abstract. Air driven motors are used in a variety of applications, for example as drives for tools in manufacturing. Pneumatic vane motors in particular feature high speed and eminent power density. In contrast to the large number of applications, only few efforts regarding dynamic simulation of these motors have been made in the past. Due to this lack of simulation studies concerning pneumatic rotating equipment, the paper presents the development and experimental validation of a one dimensional simulation model for pneumatic vane motors in Matlab/Simulink. The model developed in the study can be used as a basis for future work on the optimization and control of pneumatic vane motors. Additionally, the model may be included in lumped parameter simulation environments to improve their accuracy in the examination of pneumatically driven rotating equipment. The validation is carried out by an experimental setup which consists of the vane motor mounted on a common shaft with a hydraulic gear pump building up the load. The paper presents a validated, one-dimensional model of the dynamic behavior of a pneumatic vane motor. This is of great importance for the simulation of rotating equipment in manufacturing driven by pneumatic vane motors. [1]

Keywords: Pneumatics, Vane Motor, Simulation

INTRODUCTION

Pneumatic vane motors are widely used in industrial applications where robustness, high power-to-weight-ratio or indifference to overload are of importance. Up to today, there are only few examples for the mathematical modelling of these motors known in literature. Most models cover only a limited bandwidth of physical effects appearing in pneumatic vane motors. Beater [2] proposes a simple model in Modelica for the dynamic behavior meant for the use in lumped parameter simulation programs. The presented model does explicitly not feature the dynamic oscillations of the driving torque, as experimentally described, e.g., by Ioannidis [1]. Another model without detailed examination of friction and leakage effects is presented by Luo [3]. Badr established a detailed mathematical description for leakage [5] as well as friction effects [6] but does not present any implementation in a simulation environment. Additionally, there are some models for vane-expanders used especially in cooling applications (cf. e.g. [4]). In these applications most effort is put into the modelling of the multi-phase flow which usually does not occur in pneumatic motors. In literature, there is some work on the dynamic analysis of rotary vane combustion engines, which can in part be used for the analysis of the dynamic behavior of pneumatic motors as well. Examples were published by Librovich et. al. in [8–10].
The Matlab/Simulink-model described in the paper gives an overview of the dynamic behavior of pneumatic vane motors including friction and leakage losses dependent on geometry, working pressure and load. Especially the modeling of leakage has deep impact on the accuracy of the simulation results.
The model includes a dynamic simulation of the rotating parts of the motor including the vanes. Pressure and temperature inside the motor chambers are simulated in dependence of the rotating angle and, therefore, the volume of each chamber, the heat transfer to the environment as well as the leakage between chambers can be evaluated.
There are different paths at which internal leakage between chambers occurs (cf. **FIGURE 1**). **TABLE 1** gives an additional overview of the main leakage paths. [4]

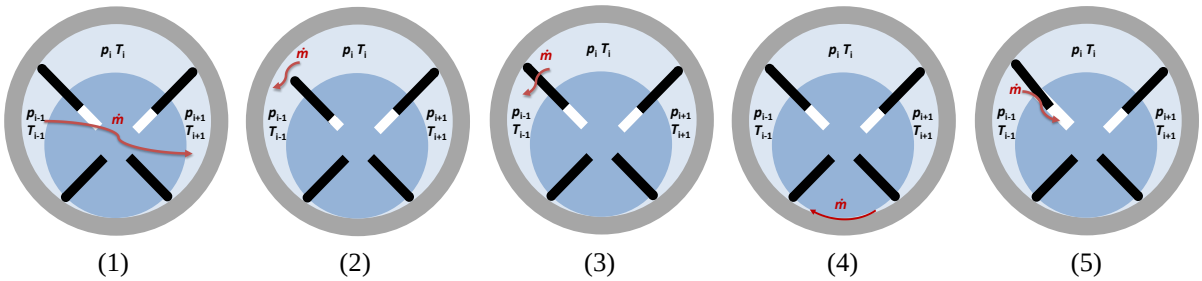

FIGURE 1 Schematic of the main paths for leakage mass flow inside the vane motor

The paper shows an estimation of the dimension of the mass flow through these paths for normal operation derived from literature. The main losses due to leakage during normal operation are calculated.
The friction torque is calculated based on the forces acting inside the motor. The friction forces between the vanes and the stator are highly dependent on the angular velocity of the motor as well as the angular position of the vanes. These dependencies and the resulting friction torque are considered in the model. An additional source of friction losses is the contact line between rotor and stator.

TABLE 1 Primary leakage paths

(1)	Axial gap between the rotor and the end plates
(2)	Radial gap between vanes and the stator
(3)	Axial gaps between the vanes and the end plates
(4)	Radial gap between the rotor and the stator
(5)	Gap between the vanes and the slots in the rotor

The driving torque is calculated as the difference between the torque generated by the pressure differences on the vanes and the friction torque acting against the movement. If the driving torque is higher than the external load, the motor accelerates. The rotating motor can be decelerated by a load torque higher than the driving torque. At stand still, a load higher than the driving torque is interpreted as static friction. Therefore, in this case, the motor stays in rest. To evaluate the angular acceleration, the variable moment of inertia is calculated in dependence of the position of the vanes.
The pressure build-up and reduction in the motor chambers is modeled as a function of the chamber geometry and the heat transfer during the rotation of the motor as well as leakage mass flow out of and into the chamber between the vanes.
As the air temperature has a high impact on pneumatic motors to avoid water condensation or icing at the outlet it is calculated during the rotational movement. This includes a model of the heat transfer between the air and the stator in dependence of the rotating velocity and the inlet conditions of the air. Multi-phase flow is not considered in the model to reduce computing time.

MATHEMATICAL MODELING

The mathematical model of the vane motor is split up in five subparts. First, a geometrical model of the motor chambers is developed. Afterwards, the pressure build-up is modeled in dependency of the chamber volume, the mass flow into and out of each chamber. To generate a valid estimation of the air mass flow, modelling of the leakage through the different paths is necessary. Once the pressure inside each chamber is known, it is possible to estimate the driving torque generated by each vane. As friction losses are very high in pneumatic vane motors, it is essential to model the friction torque in dependency of the rotary position and velocity. The modelling of these subsystems is illustrated in the following. Afterwards, specific results of the simulations carried out in the study are shown.

Geometrical Model

FIGURE 2 shows the cross sectional area A_{ch} of one chamber of the motor. To evaluate the change of volume during the rotational movement, the distance $R_{\mathrm{V}}(\varphi)$ between the rotational axis of the rotor and the inner wall of the stator has to be calculated as a function of the rotational angle φ shown in **FIGURE 2** (c). The calculation of A_{ch} is conducted under the assumption that the contact point between vane and stator always lies in the tip of the vane.

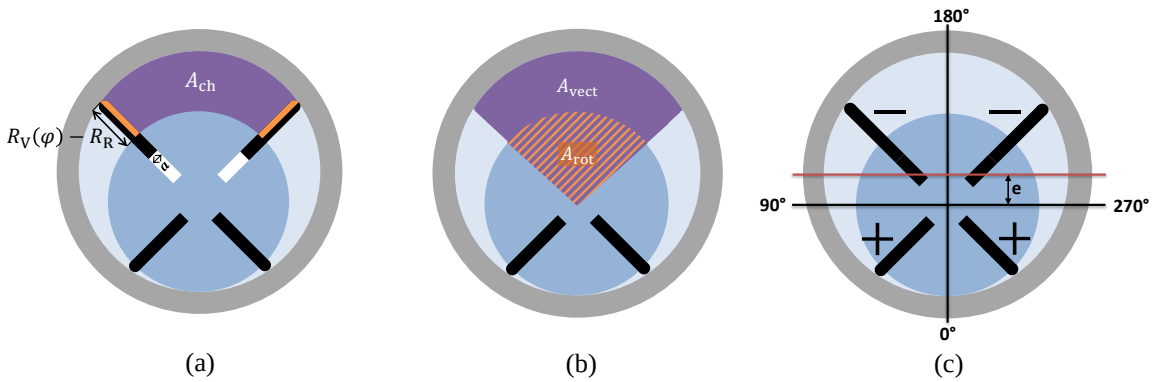

FIGURE 2 Calculation of the cross sectional area between two vanes

$R_V(\varphi)$ can be calculated by equation (1) with the eccentricity e, the rotational angle φ and the stator radius R_S.

$$R_V(\varphi) = -e \cdot \cos(\varphi) + \sqrt{R_S^2 - (e \cdot \sin(\varphi))^2} \tag{1}$$

First, the area A_{vect} between vanes 1 and 2 depicted in purple in **FIGURE 2** (b) is calculated by equation (2).

$$A_{Vect} = \frac{1}{2} \cdot \int_{\varphi_1}^{\varphi_2} R_V(\varphi)^2 d\varphi \tag{2}$$

Due to the square root term in equation (1), equation (2) has two different solutions depending on the angle φ as shown in **FIGURE 2** (c). Equations (3) and (4) show the "positive" and "negative" solution for $R^2_{V(\varphi)}$ which then are inserted in equation (2).

$$R^2_{V(\varphi)_+} = e^2 \cdot \cos(2\varphi) + R_S^2 + 2 \cdot e \cdot \sqrt{R_S^2 \cdot \left(\frac{1+\cos(2\varphi)}{2}\right) - e^2 \cdot \left(\frac{1}{8} - \frac{\cos(4\varphi)}{8}\right)} \tag{3}$$

$$R^2_{V(\varphi)_-} = e^2 \cdot \cos(2\varphi) + R_S^2 - 2 \cdot e \cdot \sqrt{R_S^2 \cdot \left(\frac{1+\cos(2\varphi)}{2}\right) - e^2 \cdot \left(\frac{1}{8} - \frac{\cos(4\varphi)}{8}\right)} \tag{4}$$

Afterwards, the area $A_{rot} = R_R^2 \, {}^{\pi}/_{N}$ between two vanes on the rotor (hatched orange in **FIGURE 2** (b)), calculated with the number of vanes N, and the area of the vanes marked in yellow in **FIGURE 2** (a) are subtracted from the area calculated in equation (2).
Multiplication with the length of the stator leads to the slope of the chamber volume shown in **FIGURE 3** for a motor with 8 vanes.

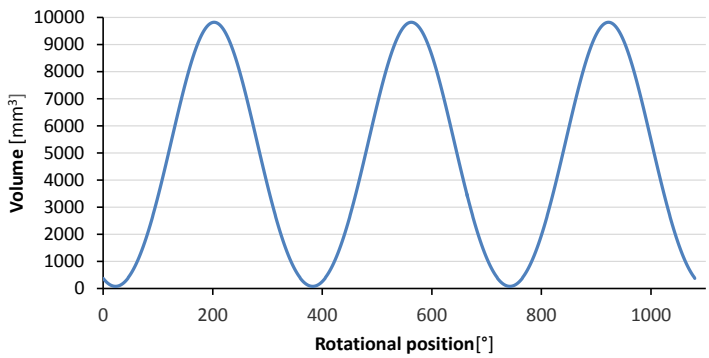

FIGURE 3 Chamber volume depending on the rotation angle

Pressure and temperature model

The pressure change in each chamber is a function of the volume change of the chamber, the mass flow into and out of the chamber as well as the air temperature. To avoid CFD-modelling of the chambers, the state variables pressure and temperature inside each chamber are considered quasi stationary and location-independent within one chamber. **FIGURE 4** shows a schematic of the p-V-diagram for one chamber during the rotation of the rotor.

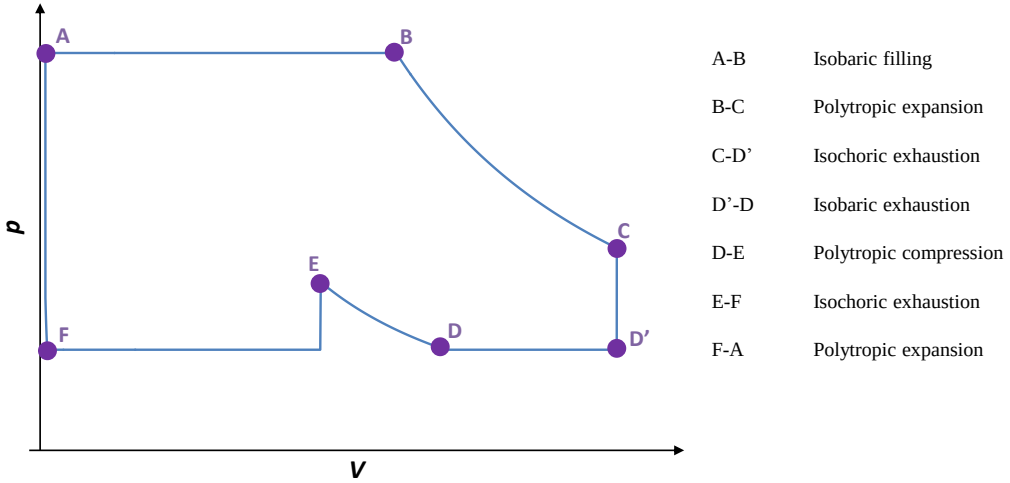

FIGURE 4: Schematic of the p-V-diagram for one chamber [2]

As the air mass inside the chamber is not constant due to leakage, the slope from 'B' to 'C' and from 'D' to 'E' cannot be modeled using the polytropic equations. Therefore, the pressure change $\dot{p}_i$ in each chamber is calculated using equation (5). [7]

$$\dot{p}_i = \dot{p}_{\dot{m}_i} + \dot{p}_{\mathrm{HE},i} + \dot{p}_{\dot{V}_i} \tag{5}$$

It is the sum of the pressure change $\dot{p}_{\dot{m}_i}$ due to mass flow into and out of each chamber, the pressure change $\dot{p}_{HE}$ due to the heat exchange between the air and the stator and the pressure change $\dot{p}_{\dot{V}}$ caused by the volume change of each chamber. These terms can be calculated according to equations (6) to (8).

$$\dot{p}_{\dot{m}_i} = \frac{k-1}{V} \cdot R \cdot \left[\sum\left(\dot{m}_{\mathrm{in},i} \cdot T_{\mathrm{in},i}\right) + \sum\left(\dot{m}_{\mathrm{out},i} \cdot T_{\mathrm{out},i}\right)\right] \tag{6}$$

$$\dot{p}_{\mathrm{HE},i} = \frac{k-1}{V} \cdot \left[\alpha \cdot \left(T_{\mathrm{stator}} - T_i\right) \cdot A_{\mathrm{wall}}\right] \tag{7}$$

$$\dot{p}_{\dot{V}_i} = -\frac{k}{V} \cdot p_i \cdot \dot{V}_i \tag{8}$$

A_{wall} describes the area on the stator between two corresponding vanes. To reduce computing time, it is approximated by the mean area (equation (9) with the number of vanes N) and considered constant for the complete revolution of the rotor. The stator temperature T_{stator} has the constant value of the environment and therewith the supply air temperature.

$$A_{\mathrm{wall}} = \left(\frac{2\pi}{N} \cdot \frac{R_S + R_R}{2}\right) \cdot L \tag{9}$$

The Nusselt number Nu delivers the heat transfer coefficient α. Using the Dittus-Boelter-equation, Nu can be calculated from the Reynolds number Re and the Prandtl number Pr according to equation (10).

$$Nu = \alpha \cdot {}^{L}/_{\lambda_{\mathrm{air}}} = 0.023 \cdot Re^{0.8} \cdot Pr^{0.3} \tag{10}$$

The temperature within each chamber is calculated by partially deriving the ideal gas equation to all time dependent terms (equation (11)).

$$\dot{T}_i = \frac{\dot{p}_i}{p_i} \cdot T_i + \frac{\dot{V}_i}{V_i} \cdot T_i - \dot{m}_i \cdot \frac{R T_i^2}{p_i \cdot V_i} \tag{11}$$

According to [1] the pressure inside one chamber is modeled as a PT_1-element when the chamber reaches the inlet to avoid a pressure jump. This approach is common for the numerical simulation of valves [7]. When the chamber pressure has reached the system pressure, its value is considered constant until the following vane leaves the inlet area.

FIGURE 5 shows the pressure in one chamber during one revolution of the motor, computed with the equations mentioned above without the consideration of leakage losses and gains. Leakage mass flows are included in the total mass flow $\dot{m}_i$ later on. The results are in good accordance to the experimental results shown by Ioannidis [1].

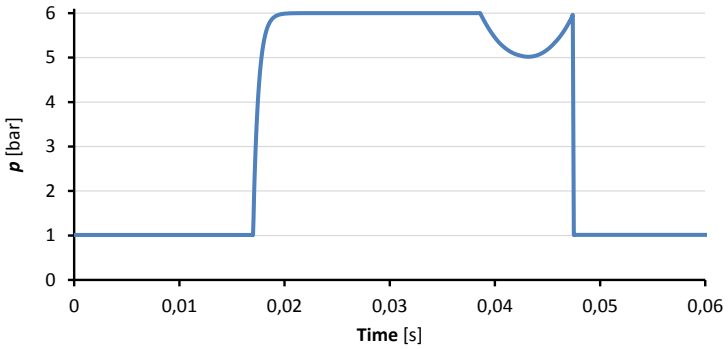

FIGURE 5 Slope of the pressure in one chamber without leakage mass flow

Leakage air flow

There are different paths through which air can leak between two adjacent chambers or from one chamber to the outlet of the motor (cf. **TABLE 1**, **FIGURE 1)** [5]. The different paths have different influences on the total leakage flow. Therefore, not all of the paths are actually modeled to reduce computing time. Due to the very small gap between the vanes and the slots in the rotor, the leakage flow through path (5) is neglected. The gap between the rotor and stator is very small while being relatively long. Additionally, the movement of the vanes and the rotor induces a flow contrary to the pressure difference. This leads to the conclusion that path (4) may be neglected as well.

The leakage mass flow through the gaps between the vanes and the stator (paths (2) and (3)) are calculated as one single ideal nozzle with a constant height of 0.1 mm to reduce computing time according to equation (12).

$$\dot{m}_{Leak,noz} = v_2 \cdot A_2 \cdot \rho_2 \tag{12}$$

Inserting the first law of thermodynamics to compute the air velocity v_2 inside the gap for each time-step from the pressure values p_2 and p_1 inside the adjacent chambers leads to equation (13) with area A_2 considered constant with a height of 0.1 mm and the length of the rotor. The density ρ_2 is derived from the ideal gas equation. [7]

$$\dot{m}_{Leak,noz} = 0.1\ \mathrm{mm} \cdot L \cdot \sqrt{2 \cdot \frac{\kappa}{\kappa - 1} \cdot p_1 \rho_1 \cdot \left(\left(\frac{p_2}{p_1}\right)^{\frac{2}{\kappa}} - \left(\frac{p_2}{p_1}\right)^{\frac{\kappa+1}{\kappa}} \right)} \tag{13}$$

In addition to the leakage flow through the gaps between the vanes and the stator (paths (2) and (3) considered above), air can leak between the rotor and the stator (path (1) in **FIGURE 1**). These losses can be modeled as an air flow through the gap between a rotating and a stationary disk. The mathematical modeling of this flow is described by Bein in [11]. The mass flow can subsequently be calculated with equation (14) with the two Fourier-coefficients, as derived in [5], described in equation (15) and (16).

$$\dot{m}_{Leak,r-s} = -\frac{(p_1 - p_2) \cdot \varepsilon_1^3}{6 \cdot v_m} \cdot \sum_{k=1}^{\infty} \Big(\big(1 - \beta^{2k}\big)(A_k \cdot \sin(k\varphi) - \sin(k\varphi - \delta)) - B_k \cdot (\cos(k\varphi) - \cos(k\varphi - \delta)) \Big) \tag{14}$$

$$\mathrm{A_k} = \frac{1}{\mathrm{k}^{2\pi(1+\beta^{2\mathrm{k}})}}\left(\frac{1}{\varphi_{\mathrm{out}} - \varphi_{\mathrm{in}} - \delta}[\cos(\mathrm{k}\varphi_{\mathrm{out}}) - \cos(\mathrm{k}(\varphi_{\mathrm{in}} - \delta)] - \frac{1}{2\pi - \varphi_{\mathrm{out}_2}}\left[1 - \cos\left(\mathrm{k}\varphi_{\mathrm{out}_2}\right)\right]\right) \tag{15}$$

$$\mathrm{B_k} = \frac{1}{\mathrm{k}^{2\pi(1+\beta^{2\mathrm{k}})}}\left(\frac{1}{\varphi_{\mathrm{out}_1} - \varphi_{\mathrm{in}} - \delta}[\sin(\mathrm{k}\varphi_{\mathrm{out}}) - \sin(\mathrm{k}(\varphi_{\mathrm{in}} - \delta)] - \frac{1}{2\pi - \varphi_{\mathrm{out}_2}}\left[1 - \sin\left(\mathrm{k}\varphi_{\mathrm{out}_2}\right)\right]\right) \tag{16}$$

Dynamic model of the rotor-vane-system

To simulate the dynamic behavior of the rotor, first it is mandatory to model the inertia $J(\varphi)$ of the rotating parts, i.e., the rotor and the vanes, in dependency of the angular position.
Using equation (17) the angular acceleration of can be calculated for each time step.

$$\ddot{\varphi}(t) = \frac{M_{\mathrm{tot}}(t)}{J(\varphi)} \tag{17}$$

As the center of gravity of each vane does not fall into the center of gravity of the rotating system, their inertia has to be calculated using Steiner's law (mass m_{v},width a_{v} and length b_{v}). This leads to equation (18) for the total moment of inertia of the rotating parts.

$$\begin{aligned} J(\varphi) &= J_{\mathrm{r}} - \sum J_{\mathrm{v},i}(\varphi) \\ &= \frac{1}{2}\cdot m_{\mathrm{r}}\cdot R_{\mathrm{r}}^2 + \sum_{i=1}^{\mathrm{N}}\left(\frac{1}{12}m_{\mathrm{v}}(a_{\mathrm{v}}^2 + b_{\mathrm{v}}^2) + m_{\mathrm{v}}d_{\mathrm{COG},i}^2\right) \end{aligned} \tag{18}$$

The radial position of each vane's center of gravity $d_{\mathrm{COG},i}$ is calculated by equation (19).

$$\begin{aligned} d_{\mathrm{COG},i} &= R_{v,i}(\varphi) - \frac{b}{2} \\ &= -e\cdot\cos(\varphi) + \sqrt{R_S^2 - (e\cdot\sin(\varphi)^2)} - \frac{b}{2} \end{aligned} \tag{19}$$

The total torque working on the rotor is calculated using equation (20)

$$M_{\mathrm{tot}}(\varphi) = M_{\mathrm{p}}(\varphi) - M_{\mathrm{fr,v-r}}(\varphi) - M_{\mathrm{fr,r-s}}(\varphi) - M_{\mathrm{load}} \tag{20}$$

which is the difference between the torque $M_{\mathrm{p}}(\varphi)$ generated by the pressure differences Δp_i over the vanes and the friction between the vanes and rotor $M_{\mathrm{fr,v-r}}(\varphi)$ and between the rotor and stator $M_{\mathrm{fr,r-s}}(\varphi)$, respectively as well as the constant load M_{load}. $M_{\mathrm{p}}(\varphi)$ is calculated by equation (21)

$$M_p = \sum_{i=1}^{N} M_i = \sum_{i=1}^{N}(\Delta p_i\cdot A_i\cdot d_i) \tag{21}$$

with the lever arm d_i and the pressurized area A_i for each vane calculated according to equations (22) and (23).

$$d_i(\varphi) = \frac{R_V(\varphi) + R_R}{2} = \frac{1}{2} \cdot \left(-e \cdot \cos(\varphi) + R_R + \sqrt{R_S^2 - (d \cdot \sin(\varphi))^2} \right) \tag{22}$$

$$A_i(\varphi) = L \cdot \left(-e \cdot \cos(\varphi) - R_R + \sqrt{R_S^2 - (d_i \cdot \sin(\varphi))^2} \right) \tag{23}$$

Friction modelling

As the output torque of the motor is highly dependent on the losses within the motor, detailed modeling of the friction is necessary to achieve reliable results.
In the study, two main sources for friction losses are considered. First, velocity proportional friction is calculated. This includes the losses caused by steady, lubricated contacts which appear mainly in the bearings.

$$M_{\mathrm{fr,r-s}}(\varphi) = \mu_{\mathrm{fr,r-s}} \cdot \dot{\varphi} \tag{24}$$

The second source for major friction losses is the contact between the vanes and the stator. The contact force and, therewith, the friction force at each vane has to be calculated for each vane separately. It can be seen in **FIGURE 6** that tilting of the vanes occurs in the slot.

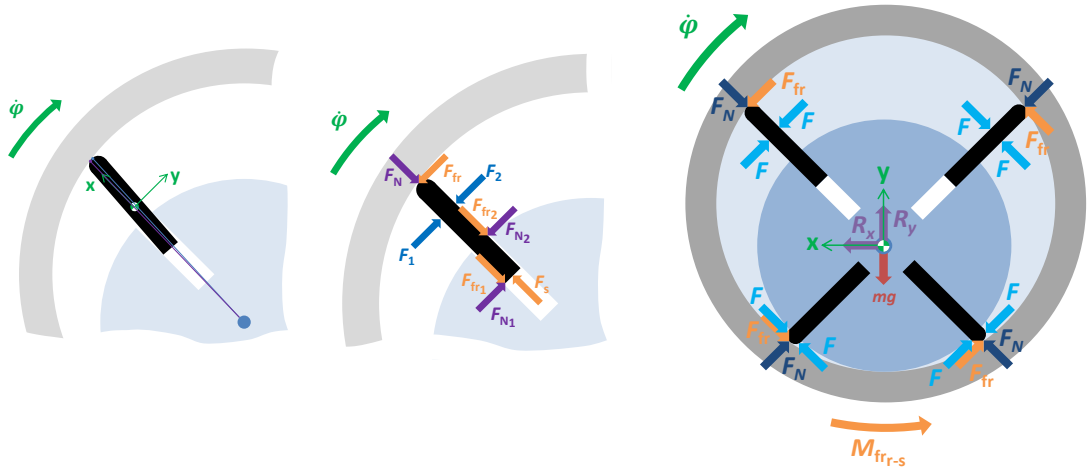

(a) (b) (c)

FIGURE 6 Vane tilting and resulting friction forces at the vane

The forces resulting from the tilting (the friction forces between the vane and the rotor $F_{\mathrm{fr},1}$ and $F_{\mathrm{fr},2}$ (cf. **FIGURE 6** (b) which are depicted as well, can be calculated for each vane in dependence of the rotational position. Solving the mechanical system (including the radial force F_{S}) leads to equation (25) for the angle-dependent friction torque, including the radial contact forces $F_{\mathrm{N},i}$ for each vane. The assumption of a permanent contact between the tip of the vane and the stator is necessary.

$$M_{\mathrm{fr,v-r}}(\varphi) = \sum_{i=1}^{\mathrm{N}} M_{(\mathrm{fr,v-r}),i} = \sum_{i=1}^{\mathrm{N}} \mu_{\mathrm{fr}} \cdot F_{\mathrm{N},i} \cdot R_{\mathrm{v}}(\varphi) = \sum_{i=1}^{\mathrm{N}} \mu_{\mathrm{fr}} \cdot F_{\mathrm{N},i} \cdot (-e \cdot \cos(\varphi) + \sqrt{R_{\mathrm{s}}^2 - (e \cdot \sin(\varphi))^2} \tag{25}$$

RESULTS & EXPERIMENTAL VALIDATION

To validate the results of the simulation study, a test rig was constructed in the IFAS lab. The test-rig consists of a reversible pneumatic vane motor with eight vanes without use of the expansion energy, i.e., the motor only has two ports for the air inlet and outlet respectively. Both ports cover a range of 90°. The inlet port starts at an angle of $\varphi_{\mathrm{in}_1} = 30°$, the outlet port begins at $\varphi_{\mathrm{out}_1} = 240°$. A hydraulic gear pump with a displacement of $V_{\mathrm{pump}} = 6\ \mathrm{cm}^3$ is used as a manually adjustable load. The load torque applied by the pump is adjusted by a

pressure relief valve with a maximum pressure of $p_{\mathrm{hy,max}} = 80$ bar. A schematic of this test rig is shown in **FIGURE 7**. The hydraulic pressure generated by the pump and the pneumatic supply pressure at the motor inlet are measured as well as the torque and the angular velocity. The motor outlet is connected to the environment. Additionally, the air flow to the motor is measured by a calorimetric mass flow sensor.

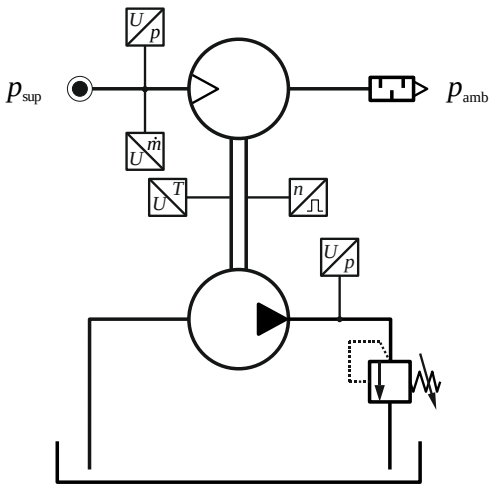

FIGURE 7 Schematic of the test rig

To validate the simulations different loads are applied to the motor working at a driving air pressure of 5 bar relative to the environment. **FIGURE 8 ff**. show exemplary results of the simulations in comparison to the experiment.

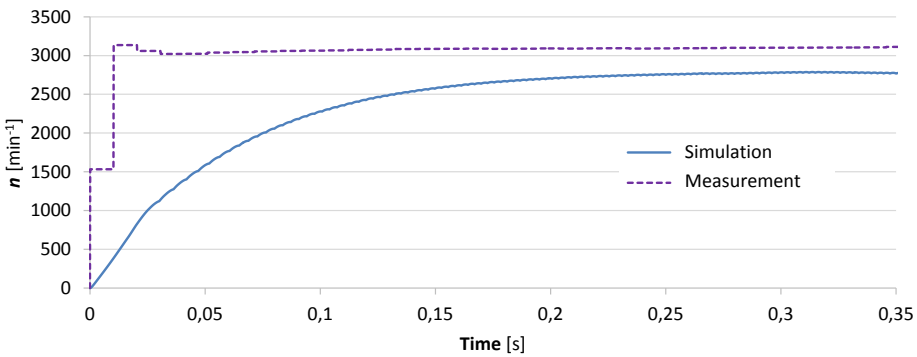

FIGURE 8 Measured (purple dashed) and simulated (blue) rotational speed for low load

It is obvious that the values for the rotational speed are in acceptable accordance (deviation around 10 %) for higher time values whereas the rise of the rotational speed in the start-up phase does not fit the experimental values. The same applies for the slope of the mean torque. The high deviations during start-up are caused by the modeling of the load torque. In the model, the load is a constant value acting right from the start of the rotational movement. In reality, the hydraulic pump first needs to build up pressure. Due to this lack of load at the beginning, the motor is able to accelerate very fast. In the simulation, a higher load slows down the acceleration at the beginning. When the pressure build-up in the hydraulic system is completed, the rotational speed stays constant. This constant value lies in a range of 8 % and 10 % to the simulated constant values at low and medium load, respectively.

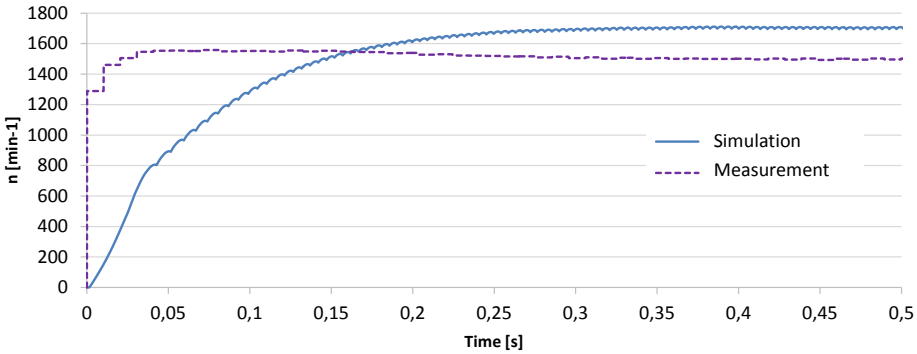

FIGURE 9 Measured (purple dashed) and simulated (blue) rotational speed for medium load

FIGURE 10 shows a comparison of the measured and simulated torque for medium load. It is obvious, that the simulation shows higher fluctuation of the torque than the experiment. Nevertheless, the mean values are in good accordance. One of the main reasons for the oscillations in the simulation is the modeling of the outlet of the motor. When the front vane reaches the outlet, the pressure falls from 6 to 1 bar in just one timestep. This leads to high numerical oscillations seen in the simulated torque. Future work on the simulation model will focus on this problem.

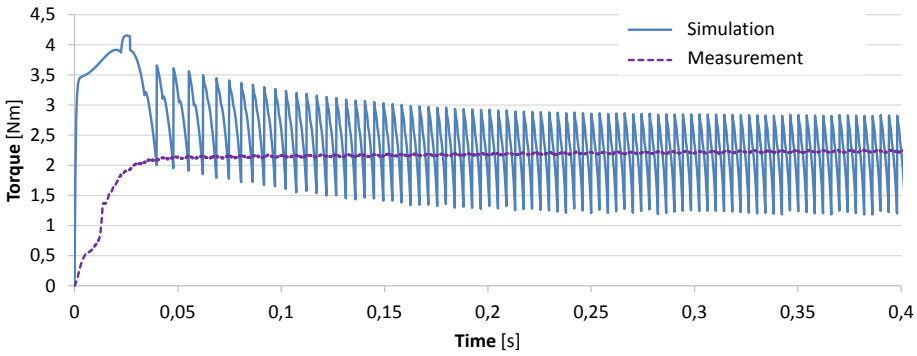

FIGURE 10 Measured (purple dashed) and simulated (blue) torque for medium load

The simulation includes only one degree of freedom for the vanes. Therefore, a loss of contact between the vanes and the stator cannot be modeled. Especially at higher loads, a lift-off of the vanes may occur. This leads to higher leakage and subsequently to a lower driving torque in the experimental setup. A lower driving torque then leads to a lower maximum speed, which shows in the results above. Future work on the simulation model will focus on this problem by adding a second degree of freedom for the vanes.

SUMMARY & OUTLOOK

The paper presents a detailed model of the dynamic behavior of pneumatic vane motors. Especially the modelling of the pressure inside each chamber including a detailed description of the leakage losses between the chambers and through the gap between rotor and stator is shown. A detailed model for the friction between the vanes and the stator in dependence from the rotational position is shown as well. In combination with the geometrical model of the inertia and the chamber volumes between the vanes, it is possible to obtain a good accordance for the steady state behavior of the motor whereas the behavior during the start-up phase lacks accuracy.

In future projects, the dynamic behavior of pneumatic vane motors should be examined more closely. Therefore, a validation of the pressure inside each chamber should be developed. Also, a more detailed mathematical description of the friction at the tips of the vanes should be added to the model. Therefore, a second degree of freedom should be added to the simulation of the vanes' positions. By doing so, it is possible to describe the loss of contact between the vanes and the stator. When the vane lifts off of the stator surface, the friction torque is reduced massively while the leakage losses increase largely. This has a large influence on the dynamic behavior at high load as well as low rotational speeds.

Detailed knowledge of the dynamic behavior can be used to implement model based control algorithms or for the simulative design of closed loop control for pneumatic motors which are mostly used in simple, open loop controlled applications today.

NOMENCLATURE

a	Width of the vane
A_{wall}	Wall area between two vanes
b	Length of the vane
e	Eccentricity of the rotor
J	Moment of inertia
k	Polytropic coefficient of air
L	Length of the motor
$m_{\mathrm{r}}, m_{\mathrm{v}}$	Mass (of the rotor/vane)
$\dot{m}$	Mass flow
N	Number of vanes
Nu	Nusselt number
p_i	Pressure within chamber i
Pr	Prandtl number
R	Specific gas constant of air
$R, R_{\mathrm{R}}, R_{\mathrm{S}}$	Radius (of the rotor/stator)
Re	Reynolds number
T_i	Air temperature within chamber i
V_i	Geometric volume of chamber i
α	Heat transfer coefficient
λ_{air}	Heat conductance of air

REFERENCES

1. IOANNIDIS I., “Servopneumatische Drehantriebe für Lageregelungen,” Dissertation, Institut für hydraulische und pneumatische Antriebe und Steuerungen, RWTH Aachen, Aachen, 1987.
2. BEATER P., “Modelling and Control of Pneumatic Vane Motors,” International Journal of Fluid Power, **5**(1), 2004, pp. 7–16.
3. LUO X., WANG J., SHPANIN L., JIA N., LIU G., and ZINOBER A. S., 2008, “Development of a Mathematical Model for Vane-type Air Motors with Arbitrary N Vanes,” *Proceedings of the World Congress on Engineering 2008*, Newswood Limited.
4. MAHMOUD A. M., SHERIF S. A., and LEAR W. E., “Frictional and Internal Leakage Losses in Rotary-Vane Two-Phase Refrigerating Expanders,” J. Energy Resour. Technol., **132**(2), 2010.
5. BADR O., PROBERT S. D., and O'CALLAGHAN P. W., “Multi-Vane Expanders: Internal-Leakage Losses,” Applied Energy, **1985**(20), 1985, pp. 1–46.
6. BADR O., PROBERT S. D., and O'CALLAGHAN P. W., “Multi-Vane Expanders: Vane Dynamics and Friction Losses,” Applied Energy, **1985**(20), 1985, pp. 253–285.
7. MURRENHOFF H., and REINERTZ O. *Fundamentals of Fluid Power: Part 2: Pneumatics*, Shaker, Aachen, 2014.
8. LIBROVICH B., TUCKER R. W., and WANG C., “On Gear Modelling in Mulitstage Rotary Vane Engines,” Meccanica, **39**(1), 2004, pp. 47–61.
9. LIBROVICH B. V., and NOWAKOWSKI A. F., “Analysis, Design, and Modeling of a Rotary Vane Engine (RVE),” J. Mech. Des., **126**(4), 2004, p. 711.
10. LIBROVICH B. V., “Dynamics of Rotary Vane Engine,” J. Mech. Des., **125**(3), 2003, p. 498.
11. BEIN M., SHAVIT A., and SOLAN A., “Nonaxisymmetric Flow in the Narrow Gap Between a Rotating and a Stationary Disk,” Journal of Fluids Engineering, **1976**(98), 1976, pp. 217–223.

